JACS Au
AN OPEN ACCESS JOURNAL OF THE AMERICAN CHEMICAL SOCIETY

pubs.acs.org/jacsau

Article

Uncovering the Kinetic Characteristics and Degradation Preference of PROTAC Systems with Advanced Theoretical Analyses

Rongfan Tang,[§] Zhe Wang,[§] Sutong Xiang, Lingling Wang, Yang Yu, Qinghua Wang, Qirui Deng, Tingjun Hou,* and Huiyong Sun*

Cite This: *JACS Au* 2023, 3, 1775−1789

Read Online

ACCESS | Metrics & More | Article Recommendations | Supporting Information

ABSTRACT: Proteolysis-targeting chimeras (PROTACs), which can selectively induce the degradation of target proteins, represent an attractive technology in drug discovery. A large number of PROTACs have been reported, but due to the complicated structural and kinetic characteristics of the target-PROTAC-E3 ligase ternary interaction process, the rational design of PROTACs is still quite challenging. Here, we characterized and analyzed the kinetic mechanism of MZ1, a PROTAC that targets the bromodomain (BD) of the bromodomain and extra terminal (BET) protein (Brd2, Brd3, or Brd4) and von Hippel-Lindau E3 ligase (VHL), from the kinetic and thermodynamic perspectives of view by using enhanced sampling simulations and free energy calculations. The simulations yielded satisfactory predictions on the relative residence time and standard binding free energy (r_p > 0.9) for MZ1 in different Brd^{BD}-MZ1-VHL ternary complexes. Interestingly, the simulation of the PROTAC ternary complex disintegration illustrates that MZ1 tends to remain on the surface of VHL with the BD proteins dissociating alone without a specific dissociation direction, indicating that the PROTAC prefers more to bind with E3 ligase at the first step in the formation of the target-PROTAC-E3 ligase ternary complex. Further exploration of the degradation difference of MZ1 in different Brd systems shows that the PROTAC with higher degradation efficiency tends to leave more lysine exposed on the target protein, which is guaranteed by the stability (binding affinity) and durability (residence time) of the target-PROTAC-E3 ligase ternary complex. It is quite possible that the underlying binding characteristics of the Brd^{BD}-MZ1-VHL systems revealed by this study may be shared by different PROTAC systems as a general rule, which may accelerate rational PROTAC design with higher degradation efficiency.

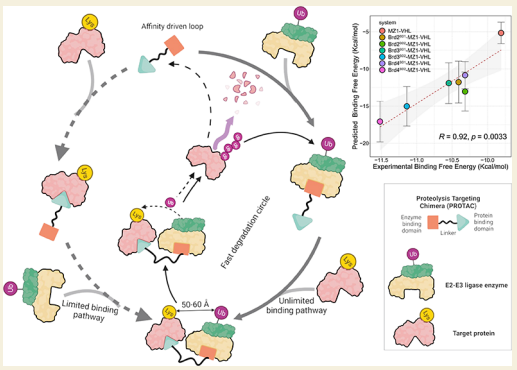

KEYWORDS: *PROTAC, Binding Free Energy Calculation, Residence Time, Umbrella Sampling, Random Accelerated Molecular Dynamics*

INTRODUCTION

Targeted protein degradation (TPD) is an emerging technique in which drugs use the cell's own proteasome system (UPS) or lysosome for target protein degradation.[1−3] Proteolysis-targeting chimera (PROTAC) proposed by Crews et al. has become one of the fastest developing targeted protein degradation technologies, which has made it possible to regulate proteins that were once considered undruggable.[2,4−6] PROTACs in clinical trials represented by ARV-110 and ARV-471 have shown significant effects in cancer therapy by targeting the degradation of the androgen receptor (AR) and estrogen receptor (ER), respectively.[7] And the first PROTAC (LC-2) targeting degradation of $KRAS^{G12C}$ shows high efficiency in attenuating the carcinogenic KRAS levels and downstream signaling in cancer cells.[8] Therefore, PROTACs have attracted wide interest and applications in the field of drug discovery in recent years.[9]

Typically, PROTACs are a class of bifunctional molecules, which are composed of an E3 ligase ligand (E3 ligand), a (warhead) ligand targeting the protein of interest (POI), and a linker connecting the above two ligands. Compared with traditional chemical drugs, PROTACs exert their drug activity through an "event-driven" rather than "occupation-driven" way, which means that the degradation activity of a PROTAC is not solely dependent on the binding affinity between the drug and the target, but closely related to the occurrence of ubiquitination labeling on the POI.[10,11] In general, ubiquitination is dependent on the formation of POI-PROTAC-E3 ligase ternary complex induced by the PROTACs. The duration of the ternary complex only needs to ensure the occurrence of ubiquitination on the POI. Once the POI is degraded, the PROTAC dissociates and

Received: April 18, 2023
Revised: May 16, 2023
Accepted: May 16, 2023
Published: June 5, 2023

https://doi.org/10.1021/jacsau.3c00195
JACS Au 2023, 3, 1775−1789

forms a new ternary complex again with another POI for the next round of degradation. In this process, the stability of the ternary complex is critical to the degradation efficiency;[12] that is, PROTACs with relatively weak interactions to the POIs may still achieve high target degradation efficiency since their ternary complexes are stable enough to induce the ubiquitination of the POIs (namely the "event-driven" case). For instance, the binding affinity of foretinib, a p38α kinase inhibitor, only achieves the micromolar level; however, the PROTAC designed based on foretinib can effectively degrade p38α kinase at the nanomolar level.[13]

Medicinal chemists usually carry out reasonable PROTAC design based on the high-affinity ligands of the E3 ligases and POIs. The traditional method is to separately design the E3 ligase ligand, the POI ligand and the proper linker. The design of the first two parts of a PROTAC is similar to that of the traditional small molecular drugs, while design of the linker needs to ensure that the PROTAC can induce the formation of a stable POI-PROTAC-E3 ligase ternary complex with proper interaction orientation between the POI and the E3 ligase, which makes the design of PROTACs more challenging than the design of traditional drugs. At present, only <5% of E3 ligases have been used for the PROTAC design,[14] and POIs achieving targeted degradation mainly include the tyrosine kinases, hormone receptors, and BET family proteins.[13,15] In addition, due to the complicated structure and dynamic characteristics of the ternary PROTAC systems, the design of PROTACs remains a great challenge. Therefore, this study expects to reveal general rules responsible for the dynamic and thermodynamic characteristics of the PROTAC ternary systems by using *in silico* techniques, so as to accelerate the rational design of PROTACs.

In the field of *in silico* computations, there have been advances in predicting the drug-target binding affinity.[16−18] However, a full understanding of the drug binding kinetics is also critical to improve drug efficacy and safety.[19−23] Generally, calculating the dissociation constant (k_{off}) or residence time ($\tau = 1/k_{off}$) is more time-consuming than determining the binding affinity, because it requires sufficient sampling of the conformational space of the drug-target dissociation process. Fortunately, Wade and co-workers proposed to use τ-random accelerated molecular dynamics (τ-RAMD) to effectively explore dissociation pathways and predict the relative residence time of drugs to their targets,[24,25] which provides us a great number of details about the (un)binding kinetics of various biological systems.[26−29]

Compound MZ1,[30] made up of the pan-BET inhibitor JQ1 (the warhead ligand),[31] a specific VHL ligand VH032 (the E3-ligase ligand),[32,33] and a three-unit PEG linker (Figure 1B), is the first PROTAC achieving degradation of the BET protein family by recruiting substrate recognition subunits von Hippel-Lindau protein (VHL). It shows selectivity for the degradation of different bromodomains (BDs) of the BET family proteins Brd2, Brd3, and Brd4 in the experiments,[15] and a number of experimental data has been deposited in this system (Brd^{BD}-MZ1-VHL),[34] facilitating one to investigate the general mechanism of formation/disintegration of the POI−PROTAC-E3 ligase ternary complex. Therefore, in this study, we carried out enhanced sampling simulations based on RAMD and umbrella sampling (US) simulations to study the binding/disintegration characteristics, the stabilization mechanism and the protein−protein interaction (PPI) features of the PROTAC systems. The results show that the residence time of PROTACs can be effectively predicted by the τ-RAMD simulation, where MZ1 tends to remain on the surface of VHL, while the BDs

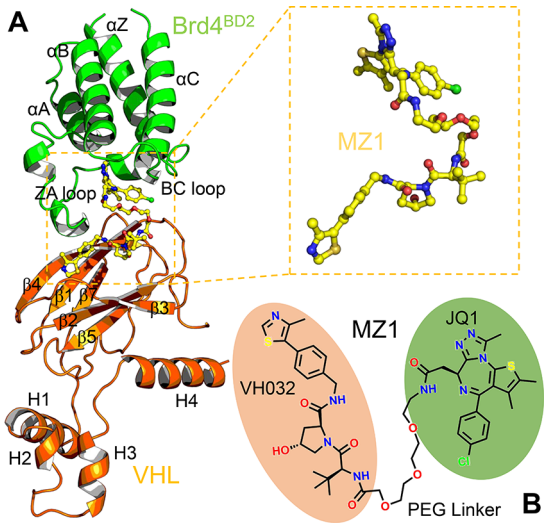

Figure 1. Typical ternary structure of a POI-PROTAC-E3 ligase system, where MZ1 (yellow) complexed with VHL (orange) and Brd4^{BD2} (green) is illustrated as an example (A) with the chemical structure of MZ1 highlighted (B).

prefer to dissociate from the surface of VHL without a specified dissociation direction, implying that MZ1 usually prefers more to form a binary complex with VHL before recruiting the BDs to form the PROTAC ternary complex. In addition, the underlying mechanism of MZ1 exhibiting higher degradation efficiency in the Brd4^{BD2}-MZ1-VHL system than the Brd4^{BD1}-MZ1-VHL system also revealed that MZ1 forms a more stable ternary complex and a more appropriate orientation in the Brd4^{BD2}-MZ1-VHL system to increase the lysine exposure of the POI (BD) for higher degradation efficiency.

MATERIALS AND METHODS

Structure Preparation

The crystal structure of the second BD of Brd4 (Brd4^{BD2}), MZ1 (a PROTAC molecule), and the von Hippel-Lindau E3 ligase (VHL) ternary complex (Brd4^{BD2}-MZ1-VHL, PDB ID: 5T35[15]) was employed for the analyses. The repeating units and water molecules were removed, and the missing flexible loops were repaired by the *Prepare Protein* module in Discovery Studio/2019 with the default parameters. Due to the lack of the crystal structures of MZ1 complexed with VHL and other BDs, the crystal structures of 3MXF, 3S92, 3S91, 3ONI,[31] and 2YEK[35] that contain different BDs and similar small molecules to MZ1 were used as the building blocks for other Brd^{BD}-MZ1-VHL system construction. The above five crystal structures were processed with a same way as that of the Brd4^{BD2}-MZ1-VHL complex, and then the five complexes with different ligand-BD were overlapped with the complex of Brd4^{BD2}-MZ1-VHL to construct the other Brd^{BD}-MZ1-VHL complexes. Besides, we treated the MZ1-VHL complex as the binary system for simulation after removing the BD protein in the Brd4^{BD2}-MZ1-VHL complex. All the modified parts of the systems were relaxed by geometry refinement and CHARMm force field optimization to clean the potential unfavorable contacts in the systems. A total of seven PROTAC systems (six Brd^{BD}-MZ1-VHL ternary systems and one MZ1-VHL binary system) were used for the following study.

Simulation System Setup

Considering the large molecular weight of a PROTAC molecule, AM1-BCC atomic charge[36] was used to handle MZ1 by using the *antechamber* module[37] in AMBER/20.[38] In the system preparation, the PROTAC molecule and protein were parametrized with the general amber force field (*gaff*, version 1.81)[39] and the ff14SB force field,[40] respectively. The ternary complexes were embedded in a TIP3P[41] water

https://doi.org/10.1021/jacsau.3c00195
JACS Au 2023, 3, 1775−1789

box extended 10 Å out of the solute in each direction. Counterions of Na^+ or Cl^- were added to neutralize the redundant charges of the systems. All the topology structures and coordinates of the PROTAC systems were built with the *tleap* module in AMBER/20.

Molecular Mechanics (MM) Minimization and MD Simulation

Before MD simulation, the prepared systems were applied for a four-step MM minimization to further optimize the unfavorable bonds or local conformations of the initial structures. In the first step, all the heavy atoms were restrained by 5 kcal/mol·Å^2 with the hydrogen atoms free for moving; then, the heavy atoms (oxygen) in water molecules and the counterions were allowed to move; subsequently, only the backbone atoms in the proteins were restrained with 5 kcal/mol·Å^2; and finally, the whole system was set free for the full minimization. Here, 5,000 steps of steepest and conjugate descent minimizations were applied to the first three steps of MM minimization, while 10,000 and 20,000 steps of steepest and conjugate descent minimizations were conducted in the fourth step of MM minimization, respectively. The real space nonbonded cutoff was set to 10 Å and the long-range electrostatic interaction was handled with the Particle Mesh Ewald (PME) algorithm.[42] The optimized structures were used for the following MD simulation.

In the phase of conventional MD (cMD) simulation, the covalent bonds containing hydrogen atoms were constrained by the SHAKE[43] algorithm and the Langevin algorithm was used to control the temperature of the system, where the collision frequency was set to 2/ps. The three-step protocol was applied to the MD simulation. First, each system was heated from 0 to 300 K during 50 ps in an NVT ensemble with the backbone atoms in the proteins restrained at 2 kcal/mol·Å^2; then each system was equilibrated for another 50 ps in an NPT ensemble with the target temperature and pressure set to 300 K and 1 atm, respectively, and the heavy atoms of the proteins restraining at 2 kcal/mol·Å^2 as well; finally, 100 ns cMD simulation was performed (T = 300 K and P = 1 atm) without any restraints. The time step was set to 2 fs, and the coordinates of the systems were recorded every 50 ps, so that a total of 2000 frames was collected in one cMD trajectory for the following analysis. All the MM minimizations and cMD simulations were performed with AMBER/20.

τ-Random Acceleration Molecular Dynamics (τ-RAMD) Simulation

RAMD has been widely applied in the exploration of potential dissociation pathways of drugs.[44−48] τ-RAMD, an extension application of RAMD, is regarded as one of the computationally efficient approaches for the prediction of drug-target residence time that plays an important role in drug efficiency.[25,49,50] At present, a number of MD sampling algorithms, such as metadynamics,[51−53] weighted ensemble (WE),[54−57] and Gaussian accelerated molecular dynamics (GaMD),[58,59] etc., have been used to predict the drug-target residence time, but the effective prediction of these methods requires either the custom parameters or very long simulation time, which undoubtedly increase the difficulty in practically characterizing the kinetic characteristics of the system. Nevertheless, RAMD simulation requires no prior knowledge of the ligand's dissociation pathway, and the only parameter needing to be customized is the range of the random force. Thus, when an appropriate random force is set, the calculated relative residence time usually goes in a reasonable range. In the spirit of RAMD simulation, an artificial force is applied to the selected part of a system (usually a ligand) with a random direction to probe whether the biased part can shift a predetermined threshold distance (r_{min}, e.g., 0.025 Å in default) along the given direction under the action of the external force within a given simulation time (e.g., 0.1 ps in default). If the biased part of the system moves enough distance in the given simulation time, the same oriented force will be continued to the subsequent simulations; otherwise, the direction of the force will be changed randomly. And when the center of mass (CoM) of the biased part of the system dissociates a certain distance from the original position, the simulation terminates.

Herein, considering that a large simulation space may be sampled in the disintegration process of the PROTAC system, all the systems were simulated with the generalized Born implicit solvent (GBIS) model in the RAMD simulations.[60−62] Since there is no long-range electrostatic calculation in the GBIS model, the real-space nonbonded cutoff was set to 16 Å. The concentration of the implicit ions was set to 0.2 M. Before RAMD simulation, each system was minimized, heated, and equilibrated in the same way as that conducted in the explicit-solvent simulations, whereas NAMD/2.14[61] in the implicit solvent model was used to facilitate the following RAMD simulations. Each system was simulated for five times to reduce the random impact on the resulted structures, and the last conformations in each system (five/system) were used as the starting points for the RAMD simulations.

In the RAMD simulation, MZ1 and BDs were defined as ligands in the six ternary systems, while MZ1 alone was set as the ligand in the binary system, with VHL used as the receptor for all the systems. To prevent drifting of the system, residues within three regions of VHL, including I147-N150, K159-L169, and E199-Q209, were constrained with 5 kcal/mol·Å^2, which are located distant from the binding surface of MZ1 and BDs and will not affect the dissociation of the ligand. An artificial force of 2.1 kcal/mol·Å was used for the RAMD simulation, which showed robust results in our prior testing. The threshold distance (r_{min}) and RAMD time interval was set to 0.025 Å and 0.1 ps (50 steps), respectively, which means that if the defined ligand can move along the given force for 0.025 Å within 0.1 ps, the direction of the force will be continued in the next round of RAMD simulation; otherwise, a random direction will be generated in the force to bias the ligand to go through other directions. The terminal distance was set to 70 Å to fully dissociate the ligand. For each starting point of the systems, 15 RAMD repeats were conducted, namely a total of 75 trajectories (5 MD repeats × 15 RAMD repeats for each system) were collected for each system for the residence time calculation and disintegration mechanism analysis. All the RAMD simulations were conducted with NAMD/2.14.

Residence Time Calculation

Theoretically, the disintegration of a biological system (rare event) follows the Poisson process, and one can estimate the effective residence time with the Poisson process to avoid influence of outlier points to the statistical result.[51,63] To characterize the Poisson process of the disintegration of a PROTAC system, the cumulative distribution function (CDF) can be used to describe the probability of observing at least one disintegration event within time t according to eq 1, where τ denotes the effective disintegration time estimated from several independent RAMD simulations.

$$P_{n\geq 1} = 1 - P_0 = 1 - \exp\left(-\frac{t}{\tau}\right) \quad (1)$$

Moreover, in order to check the sampling quality of the RAMD simulations, the two-sample Kolmogorov−Smirnov (KS) test was used to compare the empirical cumulative distribution function (ECDF) derived from the RAMD simulations and its theoretical cumulative distribution function (TCDF, that is fitted from the ECDF with the minimum variance).[63] A large p-value (e.g., > 0.05) means no statistical difference between the ECDF and TCDF, and the statistics of the samples obeys the Poisson process. Here, the computation of residence time was mainly according to the protocol proposed by Wade.[25] We conducted the KS test by using samples in each replica of the five initial structures, which shows a higher p-value in the KS test, and averaged the results to represent the estimated residence time. The detailed KS test results can be found in Figure S1 in the Supporting Information.

Umbrella Sampling

Umbrella sampling (US) has shown efficiency for studying binding free energy and kinetic details in exploring drug binding/dissociating pathways.[64−66] Here, in order to fully capture the thermodynamic and kinetic characteristics of a PROTAC interacting with the POI and E3 ligase, US was performed on the seven PROTAC systems based on the disintegration trajectories of the RAMD simulations.

In the spirit of US simulation, an external potential is employed to bias the system from one thermodynamic state (e.g., bound-state

https://doi.org/10.1021/jacsau.3c00195
JACS Au 2023, 3, 1775−1789

system) to another (e.g., free-state system) along a predefined reaction coordinate (RC).[67] In practice, the RC is usually divided into a series of pieces (named windows) to speed up the convergence of the sampling, where harmonic potential (ω) with equal or different force constant (K) is usually applied to each window to bias the sampling (eq 2), with $\omega_i(\xi)$ and ξ_i^{ref} representing the biasing potential at a certain position (ξ) of the RC and the reference position in window i, respectively.

$$\omega_i(\xi) = \frac{K}{2}(\xi - \xi_i^{\mathrm{ref}})^2 \tag{2}$$

In this study, several dissociation pathways revealed by the RAMD trajectories were employed for the US simulation in each system (5−6 trajectories for each system). A similar definition of the ligand as that of the RAMD simulation was applied in the US simulation, with the CoM distance between the heavy atoms of the ligand and the Cα atoms of residues within 5 Å of MZ1 (a part of ligand) defined as the RC. The RC position derived from each frame of the RAMD trajectory was used as the reference position for the US simulation. We took the last frame of the equilibrated phase MD simulation (before the RAMD simulation) as the initial structure for the US simulation, and then the frame whose distance was closest to the expected distance in the RAMD trajectory was used as the initial structure for the next window US simulation. Here, an average of ∼1.0 Å interval along the RC was set between two adjacent windows (Table S1), with the interval closer to each other at the beginning of the ligand's dissociation (∼0.5 Å/interval, bound-state), while farther from each other as the ligand dissociates to the solvent (∼2.0 Å/interval, free-state). Meanwhile, the root-mean-square deviation (RMSD) between two adjacent windows of the initial conformations of the ligand was kept within 3 Å to prevent too much conformational change of the ligand. For sufficient convergence of the system, 10 cycles of 1 ns-US simulation were conducted for each window (namely, 1 ns × 10 cycles × ∼45 windows for each RAMD trajectory). The weighted histogram analysis method (WHAM)[68,69] was applied to calculate the potential of mean force (PMF) by converting the biased probability distribution to a normal one along the RC. The detailed window information on the US simulation can be found in Table S1. All the PMF curves were shifted with the minimum RC point at zero. The average PMF was estimated based on the 6−10 rounds of US samples with the last 10 Å of the PMF used for the PMF depth calculation. The standard deviation was estimated based on the 6−10 rounds of PMFs with the last 10 Å of the PMF as well. All the US simulations were performed with the *pmemd.cuda* module in AMBER/20.

To calculate the standard binding free energy ($\Delta G^{\circ}_{\mathrm{US}}$) of the system, here, we applied Henchman's scheme[70] to correct the PMF depth ($\Delta \mathrm{PMF}_{\mathrm{US}}$) of the PMF curve without using additional constraints (eq 3):[71,72]

$$\Delta G^{\circ}_{\mathrm{US}} = \Delta \mathrm{PMF}_{\mathrm{US}} - RT \ln\left(\frac{L_b A_u}{V^{\circ}}\right) \tag{3}$$

$$L_b = \int_{\mathrm{bound}} \exp\left(\frac{-\Delta \mathrm{PMF}_{\mathrm{US}}(\xi)}{RT}\right) \mathrm{d}\xi \tag{4}$$

where the second term of eq 3 is associated with the standard volume (V° = 1661 Å^3), the cross-sectional area (A_u) detected by the unbound ligand (calculated by πR^2 with R = 20 and 10 Å for BD and MZ1, respectively), and the bound length (L_b) calculated by the configurational integrals of the PMF curve along the ligand-bound region of the RC ξ (eq 4).

Bound-State and Kinetic-State Analyses Based on MM/GBSA Calculation

Here, Molecular Mechanics/Generalized Born Surface Area (MM/GBSA) was used to analyze the binding characteristics of the cMD and US trajectories, which has been widely applied in various biological systems, such as protein−ligand,[73−76] protein−protein/peptide,[77,78] and protein−RNA[79] systems. The calculation of MM/GBSA binding free energy follows the below formulas:

$$\Delta G_{\mathrm{bind}} = \Delta G_{\mathrm{com}} - (\Delta G_{\mathrm{rec}} + \Delta G_{\mathrm{lig}}) \tag{5}$$

$$G_{\mathrm{bind}} = \Delta H - T\Delta S \approx \Delta E_{\mathrm{MM}} + \Delta G_{\mathrm{sol}} - T\Delta S \tag{6}$$

$$\Delta E_{\mathrm{MM}} = \Delta E_{\mathrm{int}} + \Delta E_{\mathrm{ele}} + \Delta E_{\mathrm{vdw}} \tag{7}$$

$$\Delta G_{\mathrm{sol}} = \Delta G_{\mathrm{GB}} + \Delta G_{\mathrm{SA}} \tag{8}$$

$$\Delta G_{\mathrm{SA}} = \gamma \Delta A + b \tag{9}$$

where ΔG_{bind} represents the binding free energy that is numerically equal to the energy difference between the protein−ligand complex (bound state) and the protein/ligand individuals (free state) (eq 5). Based on the second law of thermodynamics, the binding free energy can also be expressed by the enthalpy and entropy changes upon protein−ligand interactions as shown in eq 6. Because of the high computational cost of the entropy ($-T\Delta S$) calculation for the ternary system, here we did not try to take entropy into consideration. The enthalpy part (ΔH) is appropriately equal to the sum of the molecular mechanics energy change (ΔE_{MM}) and the solvation free energy change (ΔG_{sol}) of the system (eq 6), where ΔE_{MM} consists of the bonded energies (ΔE_{int} including the bond, angle, and dihedral energies) that can be canceled out here since the single MD trajectory protocol was applied for the end point binding free energy calculation due to the convergence issue,[71] and the nonbonded electrostatic (ΔE_{ele}) and van der Waals (ΔE_{vdW}) interactions (eq 7). What is noteworthy is that ΔE_{MM} only represents the energy of a system in vacuum and thus the introduction of the solvation energy (ΔG_{sol}) into the total free energy change makes the calculated energy closer to one in the physiological state. The solvation free energy can be decomposed into the polar (ΔG_{GB}) and nonpolar (ΔG_{SA}) parts (eq 8), in which the former can be estimated by a number of algorithms, represented by the Poisson−Boltzmann (PB) equation[80] and the Generalized Born (GB) model,[81] and the latter can usually be fitted by a linear equation to the solvent accessible surface area (*SASA*) (eq 9). Here, we applied Onufriev's GB model[82] for the polar solvation energy calculation with the interior (solute) and exterior dielectric (solvent) constants set to 1 and 80, respectively, and used the LCPO algorithm[83] for the ΔA estimation with the parameters of γ and b set to 0.0072 and 0, respectively. All the calculations were performed by the *MMPBSA.py* module[84] in AMBER/20.

Moreover, since the thermodynamic information on the ligand in microenvironment during the binding/dissociating process is beneficial to further understand the mechanism of action, here the kinetic energy information on the PROTAC system was characterized by the pathway analyzing method *Kinetic Residue Energy Analysis* (KREA),[72] which maps the energetic profile into individual residues along the dissociation pathway through MM/GBSA decomposition. Here, all the US snapshots were mapped according to the US RC with the energy terms ΔE_{vdW}, ΔE_{ele}, and ΔG_{GB} calculated by the above MM/GBSA protocol, and ΔG_{SA} estimated by the ICOSA algorithm.[85]

Solvent Accessible Surface Area (SASA) Analysis of the Protein Surface

The *SASA* of the system was estimated by the Shrake-Rupley algorithm[86] in PYMOL. To calculate the buried surface areas (BSA) of lysine on POI in the formation of the ternary complex, the POI in the ternary complex was separated, and the change of *SASA* between the individual POI and the POI in ternary complex was calculated for each lysine residue.[87]

H-Bond Frequency Computation

In this study, an H-bond was defined with the donor−acceptor (D-A) distance ≤3.0 Å and the angle of D-H-A ≤ 20°. The number of H-bonds were counted throughout the RAMD trajectories to calculate the H-bond frequency. All of the analyses were performed with the *Hydrogen Bonds* plugin (version 1.2) in VMD/1.9.2.[88]

https://doi.org/10.1021/jacsau.3c00195
JACS Au 2023, 3, 1775−1789

Table 1. Summary of the Binding Free Energy and Residence Time Estimated from MD Simulation

PROTAC	system	POI	K_D (nM)	K_{off} (s^{-1})	relative residence time (ns)	$\Delta G_{MZ1\text{-}BD}$ (kcal/mol)[a]	$\Delta G_{MZ1\text{-}VHL}$ (kcal/mol)[b]	ΔPMF_{US} (kcal/mol)[c]	ΔG°_{US} (kcal/mol)[d]
MZ1	binary		66	0.019	0.16 ± 0.049			−5.63 ± 1.44	−5.17 ± 1.44
	ternary	$Brd2^{BD1}$	24	>1	0.14 ± 0.049	−34.62	−42.64	−9.41 ± 2.81	−11.78 ± 2.81
	ternary	$Brd3^{BD1}$	19	>1	0.12 ± 0.040	−35.53	−45.53	−9.15 ± 2.74	−11.92 ± 2.74
	ternary	$Brd4^{BD1}$	28	>1	0.12 ± 0.040	−32.13	−46.22	−6.76 ± 1.83	−10.85 ± 1.83
	ternary	$Brd2^{BD2}$	28	0.01	0.16 ± 0.049	−38.78	−45.71	−10.55 ± 2.62	−13.04 ± 2.62
	ternary	$Brd3^{BD2}$	7	0.12	0.14 ± 0.049	−40.82	−44.19	−12.02 ± 2.65	−15.03 ± 2.65
	ternary	$Brd4^{BD2}$	3.7	0.006	0.16 ± 0.049	−41.15	−43.70	−14.85 ± 2.73	−17.09 ± 2.73
					r_p = 0.92			r_p = 0.93	r_p = 0.92

[a]$\Delta G_{MZ1\text{-}BD}$ denotes the binding free energy between MZ1 and the POI (estimated from MM/GBSA). [b]$\Delta G_{MZ1\text{-}VHL}$ represents the binding free energy between MZ1 and VHL (estimated from MM/GBSA). [c]Binding free energy estimated from the PMF depth of the US simulaiton. [d]Absolute binding free energy estimated from the Henchman's scheme based on the PMF curves.[70]

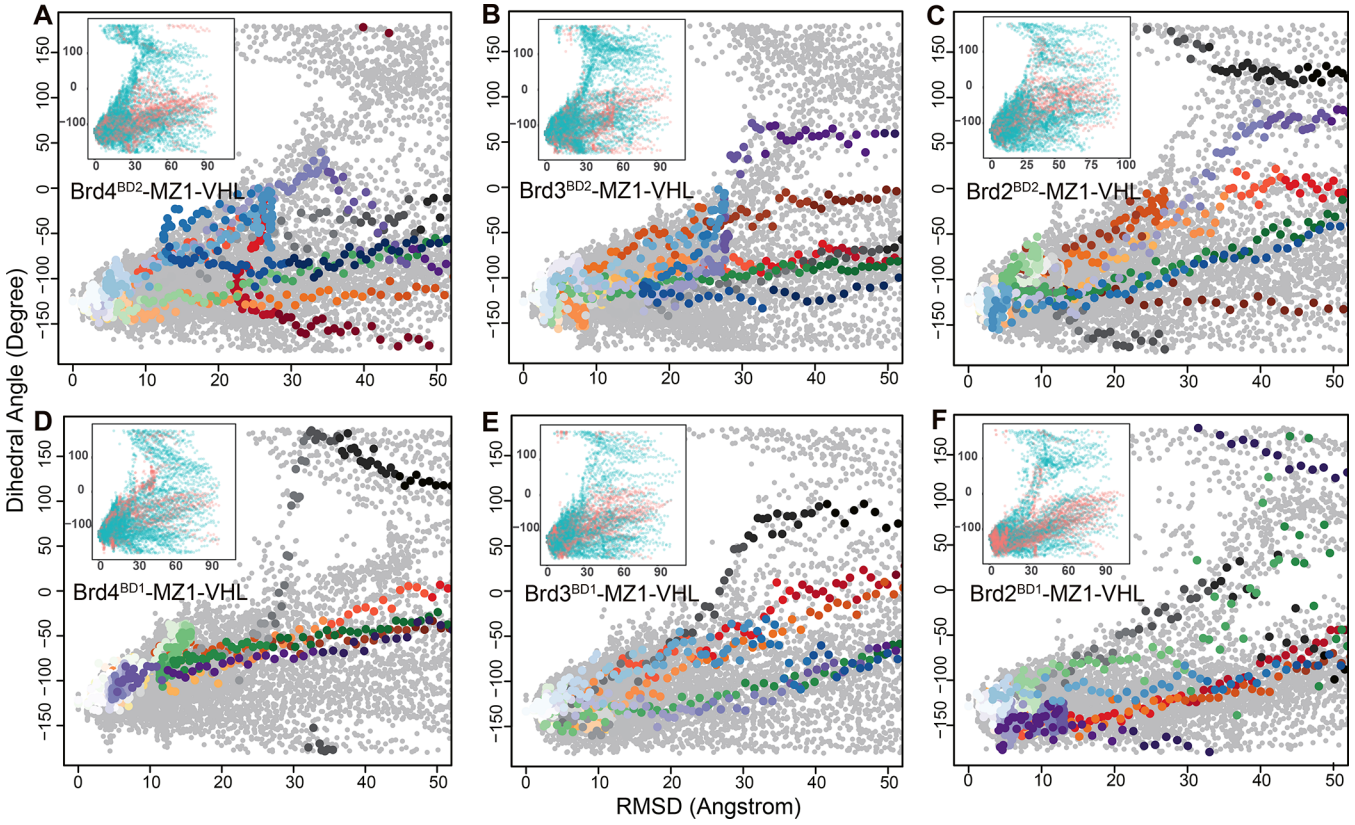

Figure 2. Changes of the dihedral angel between Brd^{BD} and VHL and RMSD of Brd^{BD} in the process of ternary structure disintegration in the 75 RAMD trajectories of the six systems, including (A) $Brd4^{BD2}$-MZ1-VHL, (B) $Brd3^{BD2}$-MZ1-VHL, (C) $Brd2^{BD2}$-MZ1-VHL, (D) $Brd4^{BD1}$-MZ1-VHL, (E) $Brd3^{BD1}$-MZ1-VHL, and (F) $Brd2^{BD1}$-MZ1-VHL. All the trajectories are classified according to whether MZ1 dissociates with BD and shown in the subgraph in each panel (cyan dots for dissociation alone and red dots for codissociation). The representative trajectories are marked with different colors in the main panels, with the remaining trajectories colored in gray.

RESULTS AND DISCUSSION

Kinetic Details of the Degradation Mechanism of the PROTAC System

Predicting the Relative Residence Time during Disintegration of the PROTAC System. The disintegration trajectories generated by the RAMD simulations were used to compute the residence time of the Brd^{BD}-MZ1-VHL ternary systems and the MZ1-VHL binary system. As shown in Table 1, a remarkable correlation (Pearson R = 0.92) is shown for the predicted residence time and the experimental data ($\log_{10}(1/k_{off})$), indicating that the τ-RAMD simulation is capable of characterizing the relative residence time and dissociation trend of a PROTAC in the ternary complex, and the trajectories are reliable for subsequent analyses. Nevertheless, it is noteworthy that the difference of the predicted relative residence time is within the standard deviation because of the too close experimental data of the systems. Therefore, we mainly compared the systems with the longest (e.g., $Brd4^{BD2}$-MZ1-VHL) and shortest (e.g., $Brd4^{BD1}$-MZ1-VHL) residence time in the following study.

MZ1 Tends to Retain on the Surface of VHL during the Disintegration Process of the Ternary Complex. Whether MZ1 dissociates with the BDs during disintegration of the Brd^{BD}-MZ1-VHL ternary complex is of great interest since it determines which protein MZ1 prefers to bind at first (BD or

https://doi.org/10.1021/jacsau.3c00195
JACS Au 2023, 3, 1775−1789

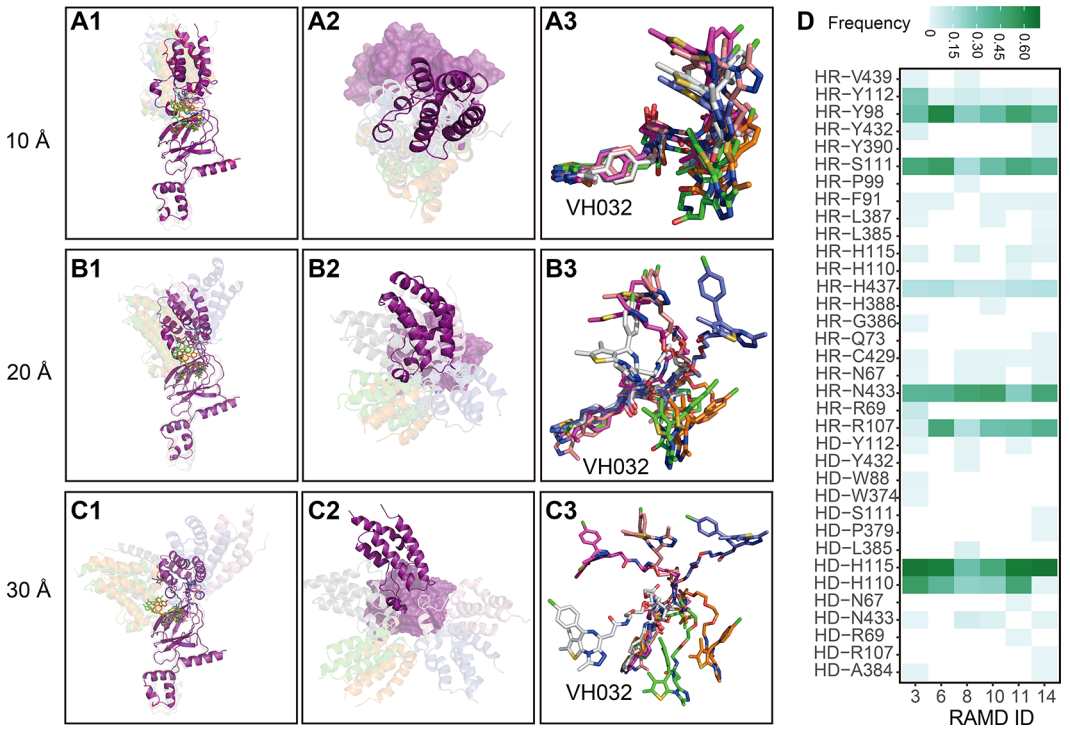

Figure 3. Structure changes of the proteins (Brd4^{BD2} and VHL) and MZ1 along the dissociation distance (RSMD of Brd4^{BD2}), (A1−A3) 10 Å, (B1−B3) 20 Å, and (C1−C3) 30 Å, where Brd4^{BD2} and MZ1 are shown in different colors in different RAMD trajectories. (D) Frequency of important H-bonds between MZ1 and the two proteins during the dissociation process in the representative RAMD trajectories.

VHL) to form the binary complex during the formation of the Brd^{BD}-MZ1-VHL ternary structure. Therefore, exploring the disintegration characteristics of the PROTAC systems can provide dynamic basis for the rational design of PROTACs.

First, we conducted 100 ns cMD simulations on the six ternary PROTAC systems and monitored the binding free energy of MZ1 to the two proteins (BD and VHL). As shown in Table 1, MZ1 exhibits stronger MM/GBSA binding affinity to VHL in all the systems ($\Delta G_{MZ1\text{-}VHL}<\Delta G_{MZ1\text{-}BD}$), indicating that MZ1 is more favorable in binding with VHL in the solution environment. Next, the 75 RAMD trajectories in each ternary system were grouped depending on whether MZ1 has dissociated together with BD (inner panel in Figure 2). The result shows that the proportion of RAMD trajectories involving codissociation of MZ1 and BD are 29/75 (Brd4^{BD2}), 16/75 (Brd4^{BD1}), 21/75 (Brd3^{BD2}), 26/75 (Brd3^{BD1}), 24/75 (Brd2^{BD2}), and 31/75 (Brd2^{BD1}) in the six PROTAC systems, accounting for a relatively small proportion, implying that MZ1 favors more in binding with VHL and tends to retain on VHL during the disintegration of the ternary structure, which is consistent with the bound-state MM/GBSA binary interaction result (Table 1). Furthermore, six representative trajectories among the 75 RAMD trajectories in the Brd4^{BD2}-MZ1-VHL system were randomly selected to investigate the structural and interacting features of the different dissociation directions of the BD. As shown in Figure 3A3−C3, when Brd4^{BD2} dissociates from the surface of VHL, MZ1 gradually disperses and extends to all the directions, with the PEG linker responsible for the high flexibility of MZ1 during the dissociation. However, the conformation of the E3-ligand part (VH032) of MZ1 targeting VHL remains relatively stable throughout the dissociation process, confirming why MZ1 tends to retain on the surface of VHL protein. And this hypothesis is further confirmed by monitoring the H-bond between MZ1 and VHL in the representative disintegration trajectories (Figure 3D), where MZ1 exhibits many H-bonds with Y98, S111, R107, H115 and H110 of VHL, while shows few H-bonds with Brd4^{BD2} (mainly with N433). Therefore, it is suggested that MZ1 prefers more to retain on VHL in most cases due to the strong H-bond interactions with VHL, and in turn indicating that MZ1 may prefer more to form binary complex with VHL at first before recruiting BD to form the ternary complex to achieve the target protein degradation.

BD Does Not Show Preferred Dissociation Direction during the Disintegration Process of the Ternary System. As shown in Figure 2, the 75 RAMD trajectories for each ternary system were plotted according to the RMSD of BD and the dihedral angle between BD and VHL. It is noteworthy that there shows no specific dissociation direction when the BD dissociates alone from the ternary complex, whereas its dissociation direction is limited to a certain range (red dots in each inner panel of Figure 2) when BD dissociates together with MZ1. This phenomenon has also been verified structurally. As shown in Figure 3A1-3B3, with the increase of dissociation distance between Brd4^{BD2} and VHL and the conformational change of MZ1, Brd4^{BD2} gradually dissociates from the surface of VHL in all directions. As a result, Brd4^{BD2} does not show an obvious preferred dissociation direction, which may be limited by the large volume of Brd4^{BD2} and its protein−protein interactions (PPIs) with VHL. Once Brd4^{BD2} breaks the strong interactions with MZ1, it slowly dissociates from the surface of VHL (Figure 3C1−C3).

Further comparison of the H-bond interactions between MZ1 and the two proteins shows that in the trajectories involving codissociation of MZ1 and Brd4^{BD2}, namely the RAMD ID of 8 and 14, a relatively higher frequency of the H-bond is shown between MZ1 and N433 on Brd4^{BD2} compared with other trajectories (Figure 3D). Moreover, the result also shows that

https://doi.org/10.1021/jacsau.3c00195
JACS Au 2023, 3, 1775−1789

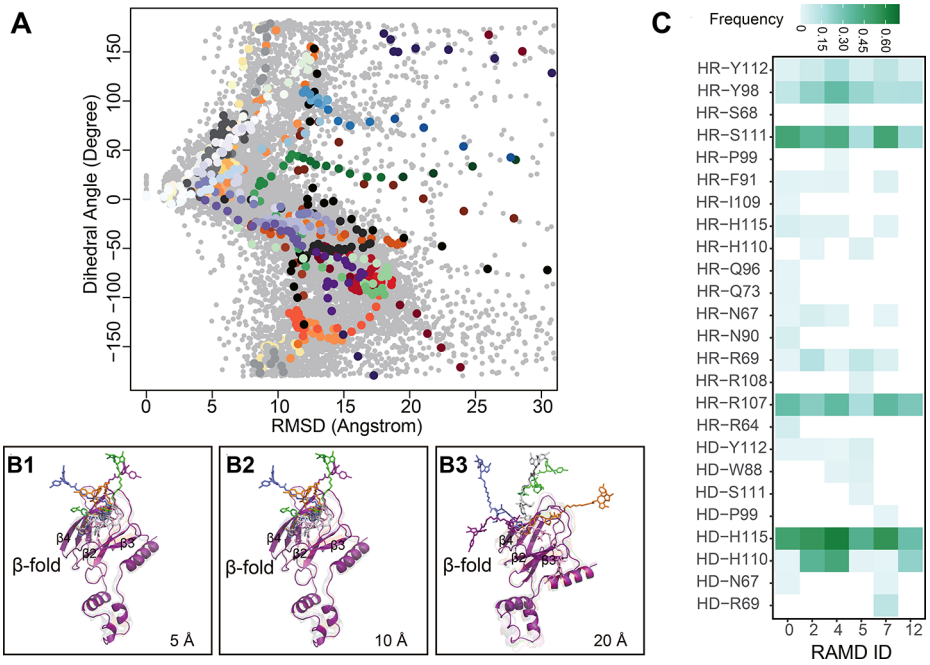

Figure 4. Changes of dihedral angle between MZ1 and VHL and RMSD of MZ1 in the dissociation of MZ1 in the 75 RAMD trajectories of MZ1-VHL binary system (A). The representative trajectories are shown in different colors, with the remaining trajectories colored in gray. The structure changes of VHL and MZ1 and the dissociation trend of MZ1 along the dissociation distance (RMSD of MZ1) are shown in (B1) 10 Å, (B2) 20 Å, and (B3) 30 Å, where MZ1 is shown in different colors for different RAMD trajectories. (C) Frequency of important H-bonds between MZ1 and VHL during the dissociation process in the representative RAMD trajectories.

MZ1 needs to try its best to prolong the interaction with $Brd4^{BD2}$ to maintain the stability of the ternary complex during the disintegration process. Therefore, based on the above characteristics of MZ1, we speculate that the dissociation characteristics are an important factor affecting the dissociation directions of the BD protein.

The Codissociation of MZ1 with BD Limits the Dissociation Direction of BD. Furthermore, we explored the dissociation details of MZ1-VHL binary system to reveal the mechanism of its influence on BD dissociation. Compared with the ternary systems, the dissociation direction of the binary system (MZ1-VHL) is more significant. As shown in Figure 4, with the dissociation of MZ1, the dihedral angle between MZ1 and VHL exhibits two distinct trends, meaning that the dissociation of MZ1 may favor a certain of directions. Since there is no BD binding with the PROTAC molecule, the parts of warhead ligand targeting BD and the linker in MZ1 are both exposed to the solvent and show a high degree of flexibility throughout the dissociation process. Consistent with the ternary systems, the stability of the binary complex mainly depends on the H-bond between MZ1 and S111, R107, H115 and H110 of VHL, implying that the E3 ligase ligand part (VH032) of MZ1 does not change its binding pattern with VHL during the formation of the ternary complex. This result also suggests the importance of choosing a proper linker for PROTAC design.

At the beginning of dissociation, the strong H-bonds between MZ1 and VHL maintain the binding mode and stabilize the conformation of VH032 in MZ1, although the flexible part of MZ1 extends to all directions. With further dissociation, MZ1 gradually overcomes the strong interactions with VHL and then dissociates along the β-folded plane in all directions. However, it is worth noting that the dissociations of MZ1 are all on the β-fold side space on the same side as β2, β3 and β4 (Figure 4B1−B3). The main reason may be that MZ1 binds to VHL at the β-fold, and therefore it is hard for it to dissociate from the opposite side of the β-fold due to its large structure. In addition, most part of the skeleton of MZ1 is exposed to the solvent region and there is no significant interaction to constrain its action in the dissociation process, therefore there is no specific dissociation pathway for MZ1 in the binary system as well. The above inference is also confirmed by the observation of the codissociation trajectories of the ternary systems (MZ1 dissociates together with BD), that is, basically all the BDs prefer to dissociate along the β-fold side space on the same side as β2, β3, and β4 in VHL because, to some extent, the strong interaction between MZ1 and BDs limits the dissociation direction of BDs, implying that, compared with the case of the MZ1-VHL binary complex interacting with BD to form the ternary complex (where no binding direction should be chosen before MZ1-VHL binding to BD), the recruitment of VHL by the MZ1-BD binary complex may be limited since an appropriate binding direction should be chosen at first for MZ1-BD to smoothly bind with VHL.

Influence of the Distinct Formation/Disintegration Mechanisms of Ternary Complex on the Degradation Efficiency. Based on the above results, we speculate that if MZ1 forms a binary complex with VHL at first during the process of forming the ternary PROTAC complex, it may be more conducive to the improvement of the degradation efficiency. This is because, on one hand, it can shorten the formation period of the next ternary PROTAC complex after BD is ubiquitinated and degraded since MZ1 prefers more to bind with VHL, and on the other hand, it may improve the path searching efficiency for the formation of ternary complex with BD, as the MZ1-VHL binary complex recruits BDs in a wider range of ways compared with the MZ1-BD binary complex binding to VHL, where the latter is usually limited by a certain directions to bind with VHL.

https://doi.org/10.1021/jacsau.3c00195
JACS Au 2023, 3, 1775−1789

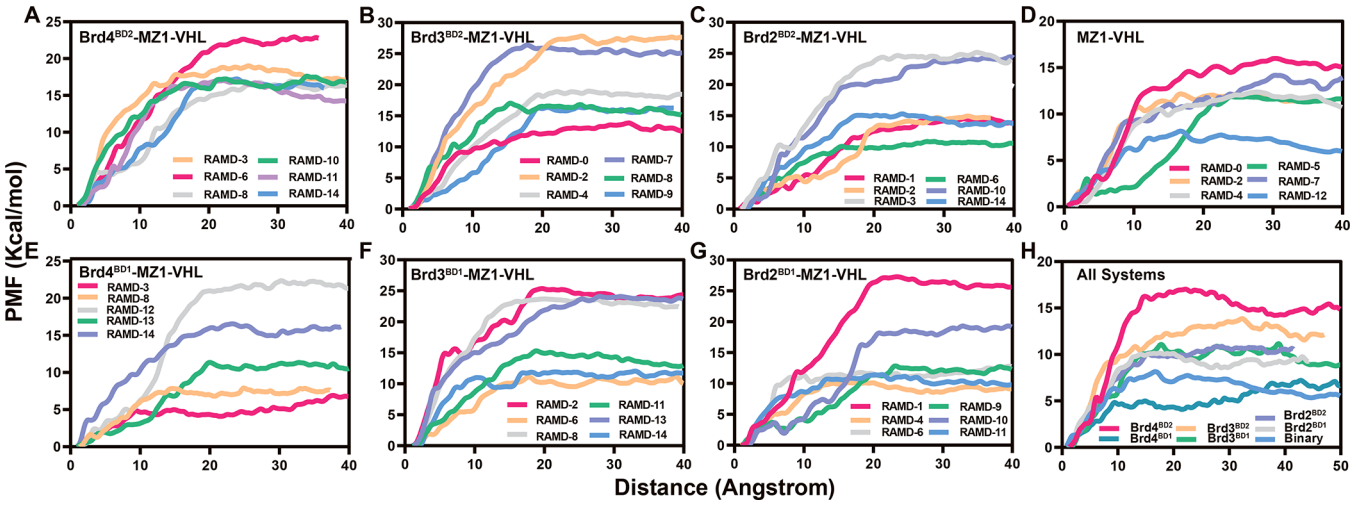

Figure 5. Average PMF based on 6−10 rounds of US simulations for the representative RAMD trajectories of the seven systems (A−G). The overall comparison of the PMFs in the seven systems is shown in panel H.

Thermodynamic Details of the Degradation Mechanism of the PROTAC System

Predicting Binding Free Energy of the PROTAC Systems during the Disintegration Process. After the initial exploration of the kinetic characteristics of the PROTAC systems, thermodynamic characteristics represented by binding free energy was also investigated for the representative RAMD trajectories, where conformations of the representative RAMD trajectories were extracted according to the dissociation distance between the defined ligand and receptor in each PROTAC system for US simulation. The potential of mean force (PMF) of each trajectory in each system was calculated (namely, 5−6 representative trajectories × 7 systems) based on 10 rounds of US simulations to guarantee the convergence of the PMF curves (namely 1 ns × ∼45 windows × 10 rounds for each RAMD trajectory). As shown in Figure 5, although a variety of dissociation pathways can be sampled by the RAMD simulation, the resulting binding free energy may be different since RAMD trajectories with different disintegration direction were selected for the investigation that may involve trajectories with high disintegration energy. Therefore, the trajectory with the lowest PMF in each system that represents the minimum free energy path (MFEP) was identified as the dominant dissociation path for the following analysis. The convergence of the MFEP PMFs can be found in Figure S2 in the Supporting Information.

As shown in Figure 6, the Pearson correlation was calculated between the standard binding free energy (ΔG°_{US}) derived from the PMF of the MFEP for each system and the experimental data, which shows a good correlation ($R = 0.92$), indicating that the MFEP is suitable for representing the dominated dissociation process of the PROTAC system. Therefore, detailed analyses were conducted on the corresponding trajectories to reveal the difference of the degradation efficiency in different PROTAC systems. Considering that the experimental data of the seven PROTAC systems are mostly on the same level, two representative systems, Brd4^{BD2}-MZ1-VHL and Brd4^{BD1}-MZ1-VHL that represent systems with higher and lower BD degradation efficiencies,[15] were employed for the following analyses. The binding mechanisms and conformational changes of the dissociation process of the system were monitored.

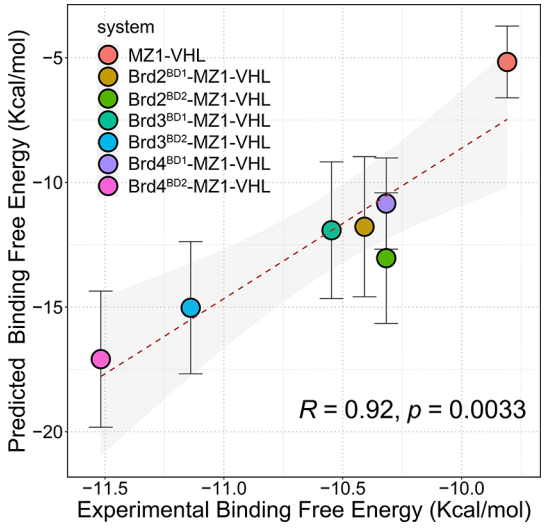

Figure 6. Pearson correlation between the standard binding free energy estimated from US simulation (ΔG°_{US}) and the experimental data (ΔG_{exp}).

Stable Ternary Structure Contributes Closely to the Degradation Efficiency of the PROTACs. The lowest point of the PMF curve corresponds to the most stable bound-state of the system. Thus, we at first extracted the structure corresponding to point A1 in the PMF curve (Figure 8A) from the US trajectory of the Brd4^{BD2}-MZ1-VHL system. Since a crystal structure (PDB ID: 5T35) has been reported for this system, we compared the RMSD difference of the PROTAC in the two ternary complexes to check whether the US simulation could explore the stable binding conformation of the PROTAC system. The result shows that the RMSD between the backbone atoms of MZ1 in the two molecules is 1.79 Å, indicating that the US simulation could explore the stable ternary complex conformation of the PROTAC systems. Based on the above analysis, we also obtained the most stable ternary structure of Brd4^{BD1}-MZ1-VHL (point A2 in Figure 8A).

By comparing the stable ternary complexes of the two systems (Brd4^{BD2}-MZ1-VHL and Brd4^{BD1}-MZ1-VHL), we found that the amino acid composition of the PPI interface in the above two systems exhibits a certain similarity. The shared residues located

https://doi.org/10.1021/jacsau.3c00195
JACS Au 2023, 3, 1775−1789

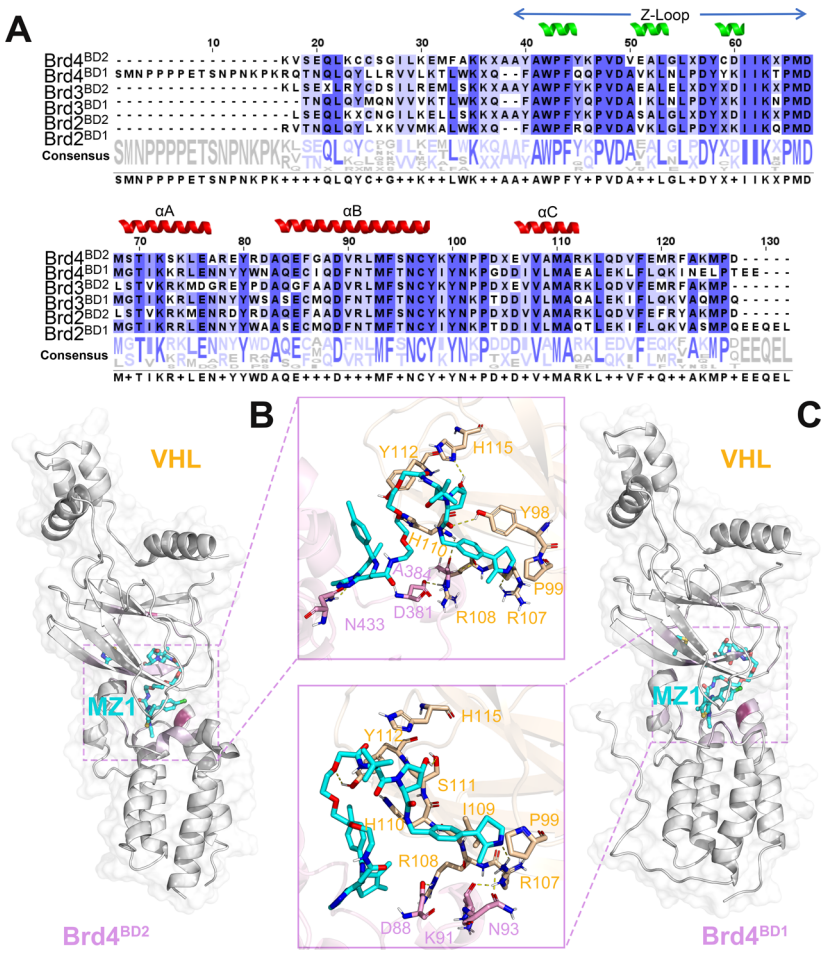

Figure 7. Sequence alignment of the six BDs (A) and structural details of the binding interfaces of Brd4^{BD2}-MZ1-VHL (B) and Brd4^{BD1}-MZ1-VHL (C), where the H-bonds are represented with yellow dash lines.

at the PPI interface of VHL in the two systems are P71, P86, W88, F91, Y98, P99, R107, R108, I109, H110, S111, Y112, H115, and W117 (orange stick model in Figure 7B and C), while the common residues forming the PPI interface on the BD of the two systems only contain W374/W42 (W81/W42) and D381/D49 (D88/D49) (pink stick model in Figure 7B and C), with the former and latter denoting the aligned residue positions in the real and simulated sequences, respectively (Figure 7A). The similarity of the protein-binding interface between the two systems further indicates that MZ1 does not change its mode to bind with VHL when inducing different BDs to form the ternary complexes, and the difference in degradation efficiency of MZ1 in different systems may arise from the difference of the binding stability between BDs and MZ1. Further monitoring of Brd^{BD}-MZ1-VHL interface interaction (Figure 7B and C) shows that three H-bonds form between VHL and BD in both systems, but in the system of Brd4^{BD2}-MZ1-VHL, MZ1 forms one additional H-bond with Brd4^{BD2}. However, no additional H-bond is formed between MZ1 and Brd4^{BD1} in the system of Brd4^{BD1}-MZ1-VHL. We speculate that the stronger H-bond interaction between MZ1 and Brd4^{BD2} makes MZ1 prefer to bind with Brd4^{BD2} than with Brd4^{BD1} and thus resulting in a more stable Brd4^{BD2}-MZ1-VHL ternary complex to enhance the degradation efficiency. To further verify our speculation, we calculated the MM/GBSA binding free energy of the stable ternary structure of the two systems and found that MZ1 exhibited stronger binding affinity to Brd4^{BD2} compared with Brd4^{BD1} (−33.57 versus −29.60 kcal/mol).

Capability of Maintaining the Stability of the Ternary Structure Contributes to the Degradation Efficiency of the PROTACs. The PMFs of BDs dissociation from the Brd4^{BD2}-MZ1-VHL (pink line) and Brd4^{BD1}-MZ1-VHL (cyan line) systems are shown in Figure 8A, where the vital states upon ligand unbinding are labeled on the PMF curves with the corresponding representative structures shown in Figure 8C−E and B, respectively, for the two systems. Moreover, the dynamic change of the interactions between MZ1 and the hot spot residues on VHL and BDs during the dissociation process were also illustrated in Figure 8F (namely, the kinetic residue energetic analysis, KREA[72]), where the residues whose interaction with MZ1 is stronger than −4.0 kcal/mol during the dissociation process were defined as hot spot residues. It is shown in Figure 8A that the tendency of the binding free energy depths (ΔPMF_{US}) obtained from the PMF curves (−14.85 ± 2.73 kcal/mol versus −6.76 ± 1.83 kcal/mol) is consistent with the experimental result that the Brd4^{BD2}-MZ1-VHL ternary complex is more stable than the Brd4^{BD1}-MZ1-VHL ternary complex (Table 1). Therefore, the formation/disintegration process of the ternary complex can be analyzed in detail.

As shown in Figure 8A, comparing the two PMFs shows that the disintegration of the Brd4^{BD2}-MZ1-VHL complex involves more transitional states than that of Brd4^{BD1}-MZ1-VHL, indicating that breaking the stability of the Brd4^{BD2}-MZ1-VHL

https://doi.org/10.1021/jacsau.3c00195
JACS Au 2023, 3, 1775−1789

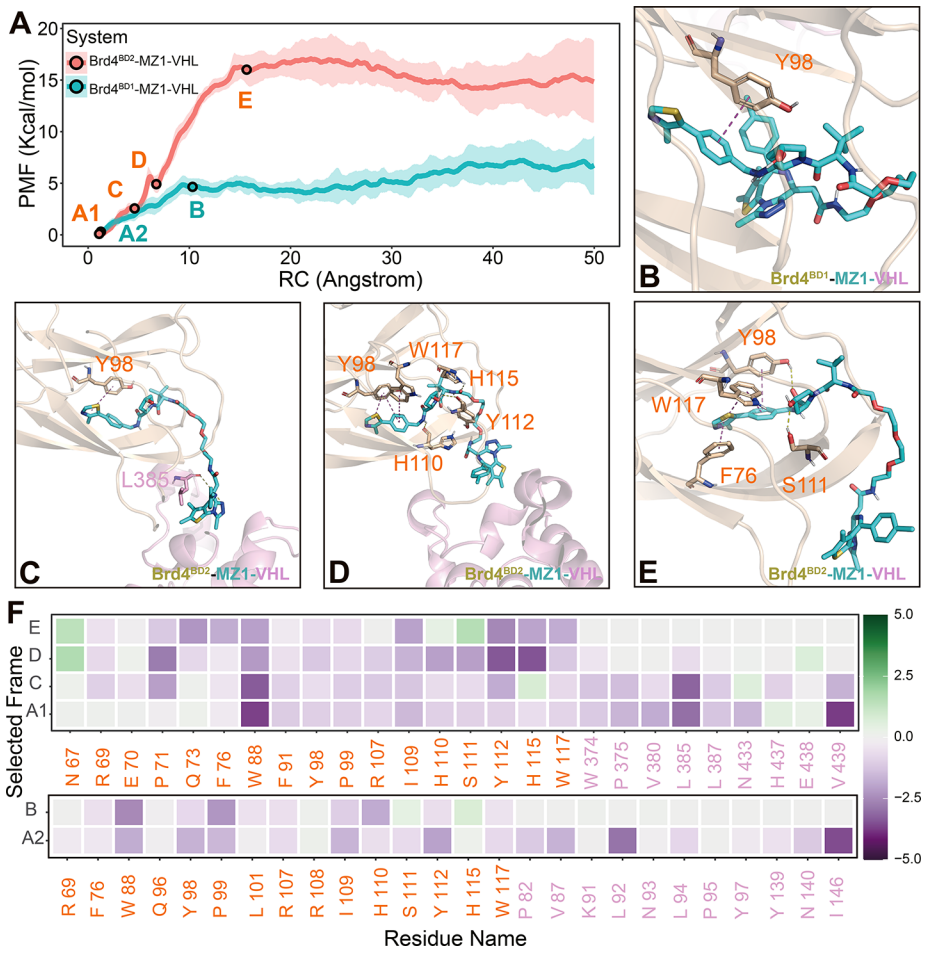

Figure 8. Structural and energetic characteristics of the disintegration process of Brd4^{BD2}-MZ1-VHL and Brd4^{BD1}-MZ1-VHL. (A) PMF curves of Brd4^{BD2}-MZ1-VHL and Brd4^{BD1}-MZ1-VHL are represented by pink and cyan lines, respectively, where the important transition states are labeled in the PMF curves and structurally illustrated (B−E) with the H-bonds and $\pi-\pi$ interactions represented by yellow and magenta dashed lines, respectively. (F) Binding free energies of key residues in the transition states, where the key residues on VHL and BD are colored by orange and pink, respectively.

ternary complex may require stepping over several energetic barriers of the transition states, while the dissociation of the Brd4^{BD1}-MZ1-VHL complex is achieved more smoothly, consistent with the experimental evidence that MZ1 is able to maintain the ternary complex of Brd4^{BD2}-MZ1-VHL for a longer residence time (Table 1), thus demonstrating a stronger degradation efficiency. Furthermore, in turn for the binding process, Brd4^{BD2} may sense the MZ1-VHL binary complex within a longer distance (∼15 Å, Figure 8A) and form a more stable ternary complex (ΔPMF_{US} = −14.85 kcal/mol) compared with Brd4^{BD1} (∼10 Å and ΔPMF_{US} = −6.76 kcal/mol).

We further investigated the transition states of the two systems structurally. In the Brd4^{BD2}-MZ1-VHL system, before the complete disintegration of the ternary complex (point E), MZ1 interacts with both VHL and Brd4^{BD2} to maintain the stability of the ternary complex, especially in the point of state C, where MZ1 maintains not only the interaction with VHL but the important H-bond with Brd4^{BD2} (Figure 8C). In terms of energetic contributions, MZ1 also exhibits stronger interactions with multiple residues on VHL and Brd4^{BD2}, such as P71 (−4.16 kcal/mol), W88 (−6.70 kcal/mol), and Y112 (−3.65 kcal/mol) on VHL and L385 (−6.41 kcal/mol) and V439 (−3.35 kcal/mol) on Brd4^{BD2} (Figure 8F). Although MZ1 does not maintain the important H-bond with Brd4^{BD2} in transition state D (Figure 8D), it still maintains the interactions with Brd4^{BD2} to some extent, such as W374 (−0.80 kcal/mol) and L385 (−1.26 kcal/mol) on Brd4^{BD2}. The disintegration of the Brd4^{BD2}-MZ1-VHL ternary complex basically reaches equilibrium in transition state E, where MZ1 remains on the surface of VHL while Brd4^{BD2} dissociates alone from the ternary complex (Figure 8E). While for the system of Brd4^{BD1}-MZ1-VHL, the stable ternary complex disintegrates at the first transition state (transition state B), where MZ1 does not exhibit a strong interaction with Brd4^{BD1} (Figure 8B). Based on the KREA, the energetic contribution of each residue in Brd4^{BD1} to MZ1 is near 0 kcal/mol (Figure 8F), meaning that the structure of Brd4^{BD1}-MZ1-VHL ternary complex is broken in the state of B.

To further investigate the difference in degradation efficiency of the PROTAC system, we compared the conformation of MZ1 in the two systems during the system disintegration. Specifically, the conformation of MZ1 changes in a relatively large way in the system of Brd4^{BD2}-MZ1-VHL, with the RMSD of MZ1 in transition states C, D, and E of 8.58, 6.58, and 8.04 Å, respectively, compared to that in its bound state (point A1). Further investigation shows that the PEG linker in MZ1 is in a fully extended state in the transition states (Figure 8C−E) compared to its bowl-shaped conformation in the bound state

https://doi.org/10.1021/jacsau.3c00195
JACS Au 2023, 3, 1775−1789

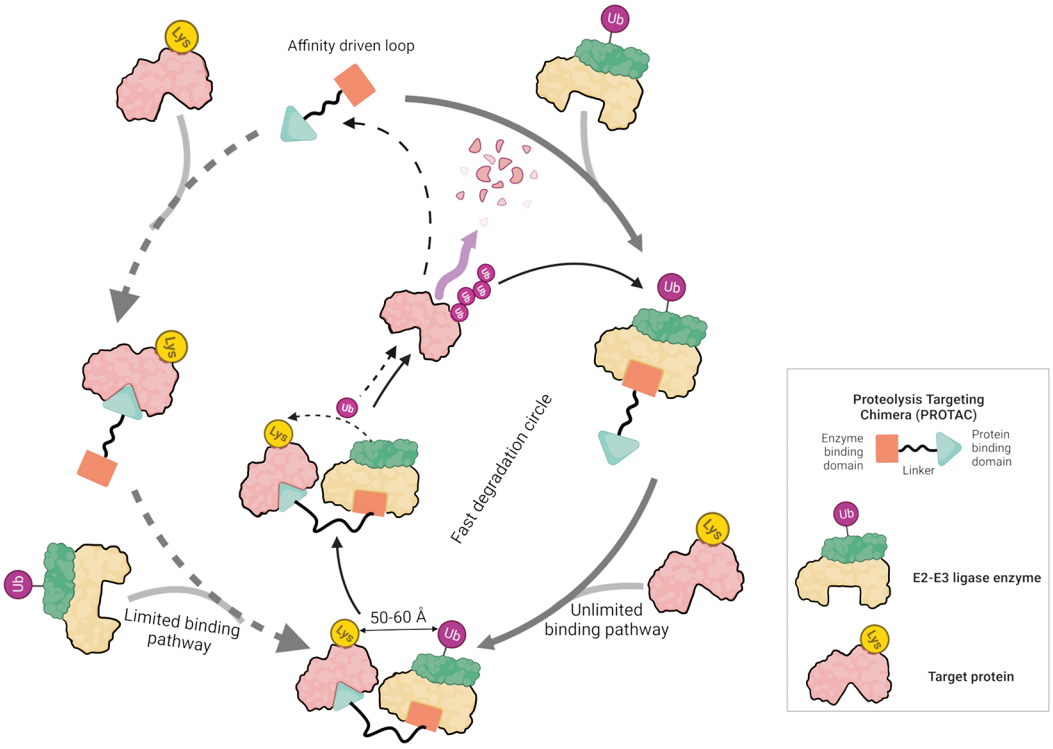

Figure 9. Schematic diagram of the ubiquitin degradation pattern of PROTAC system. The PROTAC binds to the target protein (POI), and the E3 ligase successively based on the binding affinity, thus forming a ternary complex with a certain tendency to achieve ubiquitination labeling and degradation of the target protein. If the affinity between PROTAC and E3 ligase is stronger, the PROTAC-E3 ligase binary complex can rapidly recruit target proteins to achieve targeted degradation of the POIs, whereas if the PROTAC has stronger affinity with the POI, then after the target protein degrades, the PROTAC needs to reform a ternary complex step by step to achieve targeted degradation.

(Figure 7B), which seems to be a conformational adjustment of the PROTAC in response to the dissociation of $Brd4^{BD2}$ (namely, the case that the PROTAC tries to maintain its interaction with $Brd4^{BD2}$ to stabilize the ternary structure as long as possible). However, in the system of $Brd4^{BD1}$-MZ1-VHL, MZ1 almost keeps in its original bowl-shaped conformation during the $Brd4^{BD1}$ dissociation process. Taking the most stable state A2 as the reference, the RMSD of state B is 5.64 Å, with the PEG linker folded in the whole process (Figure 8B), indicating that the relatively weak binding affinity between $Brd4^{BD1}$ and the POI-ligand part of MZ1 may leave the MZ1-VHL binary complex unable to fully participate in grasping (or binding with) the POI when the ternary complex disintegrating (or forming).

PROTAC with Higher Degradation Efficiency Needs to Ensure Its Appropriate Binding Orientation for Adequately Exposing Lysine on the Surface of the Target Protein. Moreover, numerous studies have shown that PROTAC inducing degradation of POIs depends on the ubiquitin labeling of lysine on the surface of POIs by the E3 ligase, implying that the POI needs to expose more (if not specific) lysine in the ternary structure to improve the degradation efficiency. Thus, we measured the total lysine SASA on the BD of the most stable $Brd4^{BD2}$-MZ1-VHL and $Brd4^{BD1}$-MZ1-VHL ternary complexes obtained from US simulation (corresponding to the minimum energetic point of the PMF curve), showing that the lysine SASA on the BD of the former is larger than that of the latter (1811.68 versus 1582.46 $Å^2$). Besides, the buried surface area (BSA) of lysine during the formation of the ternary complex was also calculated, in which the BSAs of BD for $Brd4^{BD2}$-MZ1-VHL and $Brd4^{BD1}$-MZ1-VHL are 50.83 and 91.53 $Å^2$, respectively. The difference of the BSA between the two systems indicates that binding of MZ1 to the $Brd4^{BD2}$-MZ1-VHL system tends to leave more lysine exposed (or reduce the BSA of lysine), making the system easier to be ubiquitin-labeled by the E3 ligase. The above result is consistent with the experimental result that the degradation efficiency of $Brd4^{BD2}$ targeted by MZ1 is higher than that of $Brd4^{BD1}$.[15]

CONCLUSION

In this work, by using enhanced sampling methodologies (mainly RAMD and US), we systematically interpreted the underlying formation/disintegration mechanism of a representative PROTAC system (Brd^{BD}-MZ1-VHL) from the kinetic and thermodynamic perspectives of view. Overall, the employed methods are reliable to predict both the kinetic (relative residence time) and thermodynamic (standard binding free energy) properties of a PROTAC system (with Pearson $R > 0.9$ in both aspects), providing us a solid basis for capturing the kinetic characteristics of the PROTAC system.

During the disintegration of the Brd^{BD}-MZ1-VHL ternary systems, MZ1 tends to remain on the surface of VHL, indicating that the PROTAC usually forms a stable binary complex with the E3 ligase (VHL) and then recruits BDs to form the ternary complex for the protein degradation. In general, the BD usually dissociates alone from the ternary complex without a specific dissociation direction, but when MZ1 dissociates together with BD, the dissociation direction of the BD will be limited to a certain extent, indicating that if the formation of the POI and PROTAC happens at first, it may, to a certain extent, limit the way to form the ternary complex. This is a good phenomenon since it indicates that the stable formation of the PROTAC-E3 ligase binary complex may facilitate it to capture the POIs and

https://doi.org/10.1021/jacsau.3c00195
JACS Au 2023, 3, 1775−1789

improve the degradation efficiency, where the PROTAC will always bind with the E3 ligase whether the POI is complete or degraded, which may save much time for the case that the PROTAC needs to seek another POI for the next round of degradation because it binds more stably with the POI compared with the E3 ligase (Figure 9).

In addition, the mechanism for the difference in the degradation efficiency of PROTACs was revealed in terms of structure and binding affinity. Whether a PROTAC can induce the formation of a stable POI-PROTAC-E3 ligase ternary complex plays an important role in its degradation capability. An efficient PROTAC should exhibit tight binding affinities to both the POI and the E3 ligase to induce them into a stable interaction complex (the ternary complex). Moreover, the interaction orientation of the POI and E3 ligase is also very important for the degradation efficiency of the POI since the formation of a ternary complex should avoid affecting more of the lysine exposure on the surface of a POI, which is necessary for the ubiquitination labeling. This speculation can also be supported by the clinically trialed ARV-110 and ARV-471 that were both designed with a rigid linker between the warhead ligand and the E3 ligase ligand to maintain an efficient interaction mode of the POIs and the E3 ligase for high efficiency degradation.[89−93] Besides, in the kinetic process of maintaining the stability of the ternary complex, a PROTAC with higher degradation efficiency may constantly adjust its conformation to prolong the stabilization time of the ternary complex, which also helps to degrade POIs with high efficiency. In summary, the proposed mechanism in this study may be helpful for the rational design of PROTACs with higher degradation efficiency.

■ ASSOCIATED CONTENT

Supporting Information

The Supporting Information is available free of charge at https://pubs.acs.org/doi/10.1021/jacsau.3c00195.

Details of the KS test of predicted residence time, convergence of MFEP PMFs, and simulation windows of US (PDF)

■ AUTHOR INFORMATION

Corresponding Authors

Tingjun Hou − *Innovation Institute for Artificial Intelligence in Medicine of Zhejiang University, College of Pharmaceutical Sciences, Zhejiang University, Hangzhou 310058 Zhejiang, P. R. China*; orcid.org/0000-0001-7227-2580; Email: tingjunhou@zju.edu.cn

Huiyong Sun − *Department of Medicinal Chemistry, China Pharmaceutical University, Nanjing 210009 Jiangsu, P. R. China*; orcid.org/0000-0002-7107-7481; Email: huiyongsun@cpu.edu.cn

Authors

Rongfan Tang − *Department of Medicinal Chemistry, China Pharmaceutical University, Nanjing 210009 Jiangsu, P. R. China*

Zhe Wang − *Innovation Institute for Artificial Intelligence in Medicine of Zhejiang University, College of Pharmaceutical Sciences, Zhejiang University, Hangzhou 310058 Zhejiang, P. R. China*

Sutong Xiang − *Department of Medicinal Chemistry, China Pharmaceutical University, Nanjing 210009 Jiangsu, P. R. China*

Lingling Wang − *Department of Medicinal Chemistry, China Pharmaceutical University, Nanjing 210009 Jiangsu, P. R. China*

Yang Yu − *Department of Medicinal Chemistry, China Pharmaceutical University, Nanjing 210009 Jiangsu, P. R. China*

Qinghua Wang − *Department of Medicinal Chemistry, China Pharmaceutical University, Nanjing 210009 Jiangsu, P. R. China*

Qirui Deng − *Department of Medicinal Chemistry, China Pharmaceutical University, Nanjing 210009 Jiangsu, P. R. China*

Complete contact information is available at: https://pubs.acs.org/10.1021/jacsau.3c00195

Author Contributions

[§]R.T. and Z.W. contributed equally to this work. Conceptualization, H.S. and T.H.; methodology, R.T., Z.W., and H.S.; analysis, R.T., Z.W., S.X., L.W., Q.W., Y.Y., Q.D., and H.S.; writing, R.T. and H.S.; supervision, H.S. and T.H.

Notes

The authors declare no competing financial interest.

■ ACKNOWLEDGMENTS

This work was supported by the National Key R&D Program of China (2021YFE0206400), the National Natural Science Foundation of China (81603031), Natural Science Foundation of Zhejiang Province (LQ21H300007), and the Young Elite Scientists Sponsorship Program by CPU (131810011 and 1132010013).

■ REFERENCES

(1) Nandi, D.; Tahiliani, P.; Kumar, A.; Chandu, D. The ubiquitin-proteasome system. *J. Biosci* **2006**, *31* (1), 137−155.

(2) Lai, A. C.; Crews, C. M. Induced protein degradation: an emerging drug discovery paradigm. *Nat. Rev. Drug Discov* **2017**, *16* (2), 101−114.

(3) Banik, S. M.; Pedram, K.; Wisnovsky, S.; Ahn, G.; Riley, N. M.; Bertozzi, C. R. Lysosome-targeting chimaeras for degradation of extracellular proteins. *Nature* **2020**, *584* (7820), 291−297.

(4) Crews, C. M. Targeting the undruggable proteome: the small molecules of my dreams. *Chem. Biol.* **2010**, *17* (6), 551−555.

(5) Bond, M. J.; Crews, C. M. Proteolysis targeting chimeras (PROTACs) come of age: entering the third decade of targeted protein degradation. *RSC Chem. Biol.* **2021**, *2* (3), 725−742.

(6) Sakamoto, K. M.; Kim, K. B.; Kumagai, A.; Mercurio, F.; Crews, C. M.; Deshaies, R. J. Protacs: chimeric molecules that target proteins to the Skp1-Cullin-F box complex for ubiquitination and degradation. *Proc. Natl. Acad. Sci. U. S. A.* **2001**, *98* (15), 8554−8559.

(7) Bushweller, J. H. Targeting transcription factors in cancer - from undruggable to reality. *Nat. Rev. Cancer* **2019**, *19* (11), 611−624.

(8) Bond, M. J.; Chu, L.; Nalawansha, D. A.; Li, K.; Crews, C. M. Targeted Degradation of Oncogenic KRAS(G12C) by VHL-Recruiting PROTACs. *ACS Cent Sci.* **2020**, *6* (8), 1367−1375.

(9) Schapira, M.; Calabrese, M. F.; Bullock, A. N.; Crews, C. M. Targeted protein degradation: expanding the toolbox. *Nat. Rev. Drug Discov* **2019**, *18* (12), 949−963.

(10) Toure, M.; Crews, C. M. Small-Molecule PROTACS: New Approaches to Protein Degradation. *Angew. Chem., Int. Ed. Engl.* **2016**, *55* (6), 1966−1973.

(11) Burslem, G. M.; Smith, B. E.; Lai, A. C.; Jaime-Figueroa, S.; McQuaid, D. C.; Bondeson, D. P.; Toure, M.; Dong, H.; Qian, Y.;

Wang, J.; et al. The Advantages of Targeted Protein Degradation Over Inhibition: An RTK Case Study. *Cell Chem. Biol.* **2018**, *25* (1), 67−77.e3.
(12) Li, K.; Crews, C. M. PROTACs: past, present and future. *Chem. Soc. Rev.* **2022**, *51* (12), 5214−5236.
(13) Bondeson, D. P.; Smith, B. E.; Burslem, G. M.; Buhimschi, A. D.; Hines, J.; Jaime-Figueroa, S.; Wang, J.; Hamman, B. D.; Ishchenko, A.; Crews, C. M. Lessons in PROTAC Design from Selective Degradation with a Promiscuous Warhead. *Cell Chem. Biol.* **2018**, *25* (1), 78−87.e5.
(14) Liu, L.; Damerell, D. R.; Koukouflis, L.; Tong, Y.; Marsden, B. D.; Schapira, M. UbiHub: a data hub for the explorers of ubiquitination pathways. *Bioinformatics* **2019**, *35* (16), 2882−2884.
(15) Gadd, M. S.; Testa, A.; Lucas, X.; Chan, K. H.; Chen, W.; Lamont, D. J.; Zengerle, M.; Ciulli, A. Structural basis of PROTAC cooperative recognition for selective protein degradation. *Nat. Chem. Biol.* **2017**, *13* (5), 514−521.
(16) Wang, E.; Sun, H.; Wang, J.; Wang, Z.; Liu, H.; Zhang, J. Z. H.; Hou, T. End-Point Binding Free Energy Calculation with MM/PBSA and MM/GBSA: Strategies and Applications in Drug Design. *Chem. Rev.* **2019**, *119* (16), 9478−9508.
(17) Williams-Noonan, B. J.; Yuriev, E.; Chalmers, D. K. Free Energy Methods in Drug Design: Prospects of "Alchemical Perturbation" in Medicinal Chemistry. *J. Med. Chem.* **2018**, *61* (3), 638−649.
(18) Torrie, G. M.; Valleau, J. P. NON-PHYSICAL SAMPLING DISTRIBUTIONS IN MONTE-CARLO FREE-ENERGY ESTIMATION - UMBRELLA SAMPLING. *J. Comput. Phys.* **1977**, *23* (2), 187−199.
(19) Copeland, R. A.; Pompliano, D. L.; Meek, T. D. Drug-target residence time and its implications for lead optimization. *Nat. Rev. Drug Discovery* **2006**, *5* (9), 730−739.
(20) Lu, H.; Tonge, P. J. Drug-target residence time: critical information for lead optimization. *Curr. Opin. Chem. Biol.* **2010**, *14* (4), 467−474.
(21) Dahl, G.; Akerud, T. Pharmacokinetics and the drug-target residence time concept. *Drug Discovery Today* **2013**, *18* (15), 697−707.
(22) Copeland, R. A. The drug-target residence time model: a 10-year retrospective. *Nat. Rev. Drug Discovery* **2016**, *15* (2), 87.
(23) Bernetti, M.; Masetti, M.; Rocchia, W.; Cavalli, A. Kinetics of drug binding and residence time. *Annu. Rev. Phys. Chem.* **2019**, *70*, 143−171.
(24) Ludemann, S. K.; Lounnas, V.; Wade, R. C. How do substrates enter and products exit the buried active site of cytochrome P450cam? 2. Steered molecular dynamics and adiabatic mapping of substrate pathways. *J. Mol. Biol.* **2000**, *303* (5), 813−830.
(25) Kokh, D. B.; Doser, B.; Richter, S.; Ormersbach, F.; Cheng, X.; Wade, R. C. A workflow for exploring ligand dissociation from a macromolecule: Efficient random acceleration molecular dynamics simulation and interaction fingerprint analysis of ligand trajectories. *J. Chem. Phys.* **2020**, *153* (12), 125102.
(26) Kokh, D. B.; Amaral, M.; Bomke, J.; Gradler, U.; Musil, D.; Buchstaller, H. P.; Dreyer, M. K.; Frech, M.; Lowinski, M.; Vallee, F.; et al. Estimation of Drug-Target Residence Times by tau-Random Acceleration Molecular Dynamics Simulations. *J. Chem. Theory Comput* **2018**, *14* (7), 3859−3869.
(27) Kokh, D. B.; Wade, R. C. G Protein-Coupled Receptor-Ligand Dissociation Rates and Mechanisms from tauRAMD Simulations. *J. Chem. Theory Comput* **2021**, *17* (10), 6610−6623.
(28) Berger, B. T.; Amaral, M.; Kokh, D. B.; Nunes-Alves, A.; Musil, D.; Heinrich, T.; Schroder, M.; Neil, R.; Wang, J.; Navratilova, I.; et al. Structure-kinetic relationship reveals the mechanism of selectivity of FAK inhibitors over PYK2. *Cell Chem. Biol.* **2021**, *28* (5), 686−698.e7.
(29) Nunes-Alves, A.; Kokh, D. B.; Wade, R. C. Ligand unbinding mechanisms and kinetics for T4 lysozyme mutants from tauRAMD simulations. *Curr. Res. Struct Biol.* **2021**, *3*, 106−111.
(30) Zengerle, M.; Chan, K. H.; Ciulli, A. Selective Small Molecule Induced Degradation of the BET Bromodomain Protein BRD4. *ACS Chem. Biol.* **2015**, *10* (8), 1770−1777.
(31) Filippakopoulos, P.; Qi, J.; Picaud, S.; Shen, Y.; Smith, W. B.; Fedorov, O.; Morse, E. M.; Keates, T.; Hickman, T. T.; Felletar, I.; et al. Selective inhibition of BET bromodomains. *Nature* **2010**, *468* (7327), 1067−1073.
(32) Galdeano, C.; Gadd, M. S.; Soares, P.; Scaffidi, S.; Van Molle, I.; Birced, I.; Hewitt, S.; Dias, D. M.; Ciulli, A. Structure-guided design and optimization of small molecules targeting the protein-protein interaction between the von Hippel-Lindau (VHL) E3 ubiquitin ligase and the hypoxia inducible factor (HIF) alpha subunit with in vitro nanomolar affinities. *J. Med. Chem.* **2014**, *57* (20), 8657−8663.
(33) Frost, J.; Galdeano, C.; Soares, P.; Gadd, M. S.; Grzes, K. M.; Ellis, L.; Epemolu, O.; Shimamura, S.; Bantscheff, M.; Grandi, P.; et al. Potent and selective chemical probe of hypoxic signalling downstream of HIF-alpha hydroxylation via VHL inhibition. *Nat. Commun.* **2016**, *7*, 13312.
(34) Roy, M. J.; Winkler, S.; Hughes, S. J.; Whitworth, C.; Galant, M.; Farnaby, W.; Rumpel, K.; Ciulli, A. SPR-Measured Dissociation Kinetics of PROTAC Ternary Complexes Influence Target Degradation Rate. *ACS Chem. Biol.* **2019**, *14* (3), 361−368.
(35) Chung, C. W.; Coste, H.; White, J. H.; Mirguet, O.; Wilde, J.; Gosmini, R. L.; Delves, C.; Magny, S. M.; Woodward, R.; Hughes, S. A.; et al. Discovery and characterization of small molecule inhibitors of the BET family bromodomains. *J. Med. Chem.* **2011**, *54* (11), 3827−3838.
(36) Jakalian, A.; Jack, D. B.; Bayly, C. I. Fast, efficient generation of high-quality atomic charges. AM1-BCC model: II. Parameterization and validation. *J. Comput. Chem.* **2002**, *23* (16), 1623−1641.
(37) Wang, J.; Wang, W.; Kollman, P. A.; Case, D. A. Automatic atom type and bond type perception in molecular mechanical calculations. *J. Mol. Graph Model* **2006**, *25* (2), 247−260.
(38) Case, D. A.; Cheatham, T. E., 3rd; Darden, T.; Gohlke, H.; Luo, R.; Merz, K. M., Jr.; Onufriev, A.; Simmerling, C.; Wang, B.; Woods, R. J. The Amber biomolecular simulation programs. *J. Comput. Chem.* **2005**, *26* (16), 1668−1688.
(39) Wang, J.; Wolf, R. M.; Caldwell, J. W.; Kollman, P. A.; Case, D. A. Development and testing of a general amber force field. *J. Comput. Chem.* **2004**, *25* (9), 1157−1174.
(40) Maier, J. A.; Martinez, C.; Kasavajhala, K.; Wickstrom, L.; Hauser, K. E.; Simmerling, C. ff14SB: Improving the Accuracy of Protein Side Chain and Backbone Parameters from ff99SB. *J. Chem. Theory Comput* **2015**, *11* (8), 3696−3713.
(41) Jorgensen, W. L.; Chandrasekhar, J.; Madura, J. D.; Impey, R. W.; Klein, M. L. Comparison of simple potential functions for simulating liquid water. *J. Chem. Phys.* **1983**, *79*, 926−935.
(42) Darden, T.; York, D.; Pedersen, L. Particle mesh Ewald: An N.log (N) method for Ewald sums in large systems. *J. Chem. Phys.* **1993**, *98* (12), 10089−10092.
(43) Ryckaert, J. P.; Ciccotti, G.; Berendsen, H. J. C. Numerical integration of the cartesian equations of motion of a system with constraints: molecular dynamics of n-alkanes. *J. Comput. Phys.* **1977**, *23* (3), 327−341.
(44) Lüdemann, S. K.; Lounnas, V.; Wade, R. C. How do substrates enter and products exit the buried active site of cytochrome P450cam? 1. Random expulsion molecular dynamics investigation of ligand access channels and mechanisms. *J. Mol. Biol.* **2000**, *303* (5), 797−811.
(45) Wang, T.; Duan, Y. Ligand Entry and Exit Pathways in the β2-Adrenergic Receptor. *J. Mol. Biol.* **2009**, *392* (4), 1102−1115.
(46) Li, W.; Fu, J.; Cheng, F.; Zheng, M.; Zhang, J.; Liu, G.; Tang, Y. Unbinding Pathways of GW4064 from Human Farnesoid X Receptor As Revealed by Molecular Dynamics Simulations. *J. Chem. Inf. Model.* **2012**, *52* (11), 3043−3052.
(47) Muvva, C.; Murugan, N. A.; Kumar Choutipalli, V. S.; Subramanian, V. Unraveling the Unbinding Pathways of Products Formed in Catalytic Reactions Involved in SIRT1−3: A Random Acceleration Molecular Dynamics Simulation Study. *J. Chem. Inf. Model.* **2019**, *59* (10), 4100−4115.
(48) Bung, N.; Roy, A.; Chen, B.; Das, D.; Pradhan, M.; Yasuda, M.; New, M. I.; Desnick, R. J.; Bulusu, G. Human hydroxymethylbilane synthase: Molecular dynamics of the pyrrole chain elongation identifies step-specific residues that cause AIP. *Proc. Natl. Acad. Sci. U.S.A.* **2018**, *115* (17), E4071−E4080.

https://doi.org/10.1021/jacsau.3c00195
JACS Au 2023, 3, 1775−1789

(49) Kokh, D. B.; Amaral, M.; Bomke, J.; Grädler, U.; Musil, D.; Buchstaller, H. P.; Dreyer, M. K.; Frech, M.; Lowinski, M.; Vallee, F.; et al. Estimation of Drug-Target Residence Times by τ-Random Acceleration Molecular Dynamics Simulations. *J. Chem. Theory Comput* **2018**, *14* (7), 3859−3869.
(50) Kokh, D. B.; Kaufmann, T.; Kister, B.; Wade, R. C. Machine Learning Analysis of τRAMD Trajectories to Decipher Molecular Determinants of Drug-Target Residence Times. *Front Mol. Biosci* **2019**, *6*, 36.
(51) Sun, H.; Li, Y.; Shen, M.; Li, D.; Kang, Y.; Hou, T. Characterizing Drug-Target Residence Time with Metadynamics: How To Achieve Dissociation Rate Efficiently without Losing Accuracy against Time-Consuming Approaches. *J. Chem. Inf Model* **2017**, *57* (8), 1895−1906.
(52) Wang, Y.; Papaleo, E.; Lindorff-Larsen, K. Mapping transiently formed and sparsely populated conformations on a complex energy landscape. *Elife* **2016**, *5*, e17505.
(53) Shekhar, M.; Smith, Z.; Seeliger, M. A.; Tiwary, P. Protein Flexibility and Dissociation Pathway Differentiation Can Explain Onset of Resistance Mutations in Kinases. *Angew. Chem., Int. Ed. Engl.* **2022**, *61* (28), e202200983.
(54) Dickson, A.; Lotz, S. D. Multiple Ligand Unbinding Pathways and Ligand-Induced Destabilization Revealed by WExplore. *Biophys. J.* **2017**, *112* (4), 620−629.
(55) Russo, J. D.; Zhang, S.; Leung, J. M. G.; Bogetti, A. T.; Thompson, J. P.; DeGrave, A. J.; Torrillo, P. A.; Pratt, A. J.; Wong, K. F.; Xia, J.; et al. WESTPA 2.0: High-Performance Upgrades for Weighted Ensemble Simulations and Analysis of Longer-Timescale Applications. *J. Chem. Theory Comput* **2022**, *18* (2), 638−649.
(56) Zuckerman, D. M.; Chong, L. T. Weighted Ensemble Simulation: Review of Methodology, Applications, and Software. *Annu. Rev. Biophys.* **2017**, *46* (1), 43−57.
(57) DeGrave, A. J.; Ha, J.-H.; Loh, S. N.; Chong, L. T. Large enhancement of response times of a protein conformational switch by computational design. *Nat. Commun.* **2018**, *9* (1), 1013.
(58) Wang, J.; Miao, Y. Protein−Protein Interaction-Gaussian Accelerated Molecular Dynamics (PPI-GaMD): Characterization of Protein Binding Thermodynamics and Kinetics. *J. Chem. Theory Comput* **2022**, *18* (3), 1275−1285.
(59) Miao, Y.; Bhattarai, A.; Wang, J. Ligand Gaussian Accelerated Molecular Dynamics (LiGaMD): Characterization of Ligand Binding Thermodynamics and Kinetics. *J. Chem. Theory Comput* **2020**, *16* (9), 5526−5547.
(60) Tanner, D. E.; Ma, W.; Chen, Z.; Schulten, K. Theoretical and computational investigation of flagellin translocation and bacterial flagellum growth. *Biophys. J.* **2011**, *100* (11), 2548−2556.
(61) Phillips, J. C.; Braun, R.; Wang, W.; Gumbart, J.; Tajkhorshid, E.; Villa, E.; Chipot, C.; Skeel, R. D.; Kalé, L.; Schulten, K. Scalable molecular dynamics with NAMD. *J. Comput. Chem.* **2005**, *26* (16), 1781−1802.
(62) Tanner, D. E.; Chan, K. Y.; Phillips, J. C.; Schulten, K. Parallel Generalized Born Implicit Solvent Calculations with NAMD. *J. Chem. Theory Comput* **2011**, *7* (11), 3635−3642.
(63) Salvalaglio, M.; Tiwary, P.; Parrinello, M. Assessing the Reliability of the Dynamics Reconstructed from Metadynamics. *J. Chem. Theory Comput* **2014**, *10* (4), 1420−1425.
(64) Su, K. H.; Wu, C. T.; Lin, S. W.; Mori, S.; Liu, W. M.; Yang, H. C. Calculation of CYP450 protein-ligand binding and dissociation free energy paths. *J. Chem. Phys.* **2021**, *155* (2), 025101.
(65) Cool, A. M.; Lindert, S. Umbrella Sampling Simulations Measure Switch Peptide Binding and Hydrophobic Patch Opening Free Energies in Cardiac Troponin. *J. Chem. Inf Model* **2022**, *62* (22), 5666−5674.
(66) Sun, H.; Chen, P.; Li, D.; Li, Y.; Hou, T. Directly Binding Rather than Induced-Fit Dominated Binding Affinity Difference in (S)- and (R)-Crizotinib Bound MTH1. *J. Chem. Theory Comput* **2016**, *12* (2), 851−860.
(67) Kästner, J. Umbrella sampling. *Wiley Interdiscip Rev. Comput. Mol. Sci.* **2011**, *1* (6), 932−942.
(68) Kumar, S.; Rosenberg, J. M.; Bouzida, D.; Swendsen, R. H.; Kollman, P. A. The weighted histogram analysis method for free-energy calculations on biomolecules. I. The method. *J. Comput. Chem.* **1992**, *13* (8), 1011−1021.
(69) Souaille, M.; Roux, B. Extension to the weighted histogram analysis method: combining umbrella sampling with free energy calculations. *Comput. Phys. Commun.* **2001**, *135* (1), 40−57.
(70) Doudou, S.; Burton, N. A.; Henchman, R. H. Standard Free Energy of Binding from a One-Dimensional Potential of Mean Force. *J. Chem. Theory Comput* **2009**, *5* (4), 909−918.
(71) Sun, H.; Li, Y.; Li, D.; Hou, T. Insight into Crizotinib Resistance Mechanisms Caused by Three Mutations in ALK Tyrosine Kinase using Free Energy Calculation Approaches. *J. Chem. Inf. Model.* **2013**, *53* (9), 2376−2389.
(72) Wang, L.; Xu, L.; Wang, Z.; Hou, T.; Hao, H.; Sun, H. Cooperation of structural motifs controls drug selectivity in cyclin-dependent kinases: an advanced theoretical analysis. *Brief. Bioinform.* **2023**, *24* (1), bbac544.
(73) Sun, H.; Li, Y.; Tian, S.; Xu, L.; Hou, T. Assessing the Performance of MM/PBSA and MM/GBSA Methods. 4. Accuracies of MM/PBSA and MM/GBSA Methodologies Evaluated by Various Simulation Protocols using PDBbind Data Set. *Phys. Chem. Chem. Phys.* **2014**, *16* (31), 16719−16729.
(74) Sun, H.; Duan, L.; Chen, F.; Liu, H.; Wang, Z.; Pan, P.; Zhu, F.; Zhang, J. Z.; Hou, T. Assessing the performance of MM/PBSA and MM/GBSA methods. 7. Entropy effects on the performance of end-point binding free energy calculation approaches. *Phys. Chem. Chem. Phys.* **2018**, *20* (21), 14450−14460.
(75) Yu, Y.; Wang, Z.; Wang, L.; Tian, S.; Hou, T.; Sun, H. Predicting the Mutation Effects of Protein-Ligand Interactions via End-Point Binding Free Energy Calculations: Strategies and Analyses. *J. Cheminform.* **2022**, *14*, 56.
(76) Tang, R.; Chen, P.; Wang, Z.; Wang, L.; Hao, H.; Hou, T.; Sun, H. Characterizing the stabilization effects of stabilizers in protein−protein systems with end-point binding free energy calculations. *Brief. Bioinform.* **2022**, *23* (3), bbac127.
(77) Weng, G.; Wang, E.; Chen, F.; Sun, H.; Wang, Z.; Hou, T. Assessing the performance of MM/PBSA and MM/GBSA methods. 9. Prediction reliability of binding affinities and binding poses for protein-peptide complexes. *Phys. Chem. Chem. Phys.* **2019**, *21* (19), 10135−10145.
(78) Wang, E.; Weng, G.; Sun, H.; Du, H.; Zhu, F.; Chen, F.; Wang, Z.; Hou, T. Assessing the performance of the MM/PBSA and MM/GBSA methods. 10. Impacts of enhanced sampling and variable dielectric model on protein-protein Interactions. *Phys. Chem. Chem. Phys.* **2019**, *21* (35), 18958−18969.
(79) Chen, F.; Sun, H.; Wang, J.; Zhu, F.; Liu, H.; Wang, Z.; Lei, T.; Li, Y.; Hou, T. Assessing the performance of MM/PBSA and MM/GBSA methods. 8. Predicting binding free energies and poses of protein-RNA complexes. *Rna* **2018**, *24* (9), 1183−1194.
(80) Honig, B.; Nicholls, A. Classical electrostatics in biology and chemistry. *Science* **1995**, *268* (5214), 1144−1149.
(81) Still, W. C.; Tempczyk, A.; Hawley, R. C.; Hendrickson, T. SEMIANALYTICAL TREATMENT OF SOLVATION FOR MOLECULAR MECHANICS AND DYNAMICS. *J. Am. Chem. Soc.* **1990**, *112* (16), 6127−6129.
(82) Onufriev, A.; Bashford, D.; Case, D. A. Exploring protein native states and large-scale conformational changes with a modified generalized born model. *Proteins: Struct., Funct., Bioinf.* **2004**, *55* (2), 383−394.
(83) Weiser, J.; Shenkin, P. S.; Still, W. C. Approximate atomic surfaces from linear combinations of pairwise overlaps (LCPO). *J. Comput. Chem.* **1999**, *20* (2), 217−230.
(84) Miller, B. R., 3rd; McGee, T. D., Jr.; Swails, J. M.; Homeyer, N.; Gohlke, H.; Roitberg, A. E. MMPBSA.py: An Efficient Program for End-State Free Energy Calculations. *J. Chem. Theory Comput* **2012**, *8* (9), 3314−3321.
(85) Gohlke, H.; Kiel, C.; Case, D. A. Insights into protein-protein binding by binding free energy calculation and free energy

https://doi.org/10.1021/jacsau.3c00195
JACS Au 2023, 3, 1775−1789

decomposition for the Ras-Raf and Ras-RalGDS complexes. *J. Mol. Biol.* **2003**, *330* (4), 891−913.
(86) Shrake, A.; Rupley, J. A. Environment and exposure to solvent of protein atoms. Lysozyme and insulin. *J. Mol. Biol.* **1973**, *79* (2), 351−371.
(87) Ribeiro, J.; Melo, F.; Schuller, A. PDIviz: analysis and visualization of protein-DNA binding interfaces. *Bioinformatics* **2015**, *31* (16), 2751−2753.
(88) Humphrey, W.; Dalke, A.; Schulten, K. VMD-Visual Molecular Dynamics. *J. Mol. Graphics* **1996**, *14* (1), 33−38.
(89) Neklesa, T.; Snyder, L. B.; Willard, R. R.; Vitale, N.; Raina, K.; Pizzano, J.; Gordon, D. A.; Bookbinder, M.; Macaluso, J.; Dong, H. Q. An oral androgen receptor PROTAC degrader for prostate cancer. *J. Clin Oncol* **2018**, *36* (6), 381.
(90) Petrylak, D. P.; Gao, X.; Vogelzang, N. J.; Garfield, M. H.; Taylor, I.; Moore, M. D.; Peck, R. A.; Burris, H. A. First-in-human phase I study of ARV-110, an androgen receptor (AR) PROTAC degrader in patients (pts) with metastatic castrate-resistant prostate cancer (mCRPC) following enzalutamide (ENZ) and/or abiraterone (ABI). *J. Clin Oncol* **2020**, *38* (15), 3500.
(91) Flanagan, J. J.; Qian, Y.; Gough, S. M.; Andreoli, M.; Bookbinder, M.; Cadelina, G.; Bradley, J.; Rousseau, E.; Willard, R.; Pizzano, J. ARV-471, an oral estrogen receptor PROTAC degrader for breast cancer. *Cancer Res.* **2019**, *79* (4), P5-04-18.
(92) Jimenez, D. G.; Sebastiano, M. R.; Caron, G.; Ermondi, G. Are we ready to design oral PROTACs®? *ADMET DMPK* **2021**, *9* (4), 243−254.
(93) Nguyen, T. T.; Kim, J. W.; Choi, H. I.; Maeng, H. J.; Koo, T. S. Development of an LC-MS/MS Method for ARV-110, a PROTAC Molecule, and Applications to Pharmacokinetic Studies. *Molecules* **2022**, *27* (6), 1977.

https://doi.org/10.1021/jacsau.3c00195
JACS Au 2023, 3, 1775−1789